

# JIGGLE: An Active Sensing Framework for Boundary Parameters Estimation in Deformable Surgical Environments

Nikhil Uday Shinde\*, Xiao Liang\*, Fei Liu, Yutong Zhang, Florian Richter, Sylvia Herbert and Michael C. Yip

**Abstract**—Surgical automation can improve the consistency and accessibility of life-saving procedures. Most surgeries require separating layers of tissue to access the surgical site, and suturing to re-attach incisions. These tasks involve deformable manipulation to safely identify and alter tissue attachment (boundary) topology. Due to poor visual acuity and frequent occlusions, surgeons tend to carefully manipulate the tissue in ways that enable inference of the tissue’s attachment points without causing unsafe tearing. In a similar fashion, we propose JIGGLE, a framework for estimation and interactive sensing of unknown boundary parameters in deformable surgical environments. This framework has two key components: (1) a probabilistic estimation to identify the current attachment points, achieved by integrating a differentiable soft-body simulator with an extended Kalman filter (EKF), and (2) an optimization-based active control pipeline that generates actions to maximize information gain of the tissue attachments, while simultaneously minimizing safety costs. The robustness of our estimation approach is demonstrated through experiments with real animal tissue, where we infer sutured attachment points using stereo endoscope observations. We also demonstrate the capabilities of our method in handling complex topological changes such as cutting and suturing.

## I. INTRODUCTION

Surgical automation has the potential to improve the accessibility of life-saving procedures in under-served communities. In recent years, the robotics community has made strides in surgical automation with the development of dVRK [1], works like STAR [2], and advancements in the automation of deformable manipulation [3], [4], [5], suturing [6], [7], blood suction [8], cutting [9] and dissection [10].

Deformable manipulation is a significant component of all surgical tasks. Large portions of surgical procedures involve safely cutting tissue to detach regions and access the surgical site, as well as suturing tissue back together. These actions actively change the structure of the surgical scene. A key step towards realizing surgical autonomy is enabling robots to understand and track these changing structures. Many previous works have aimed to take this step solely through 3D scene reconstruction [11], [12], [13], [14]. However, these works are insufficient to enable safe interaction as they fail to estimate and track the change in underlying tissue structures and provide an understanding of how aggressively the tissue is being manipulated. The key to enabling safer surgical autonomy is an interactive approach to track and control

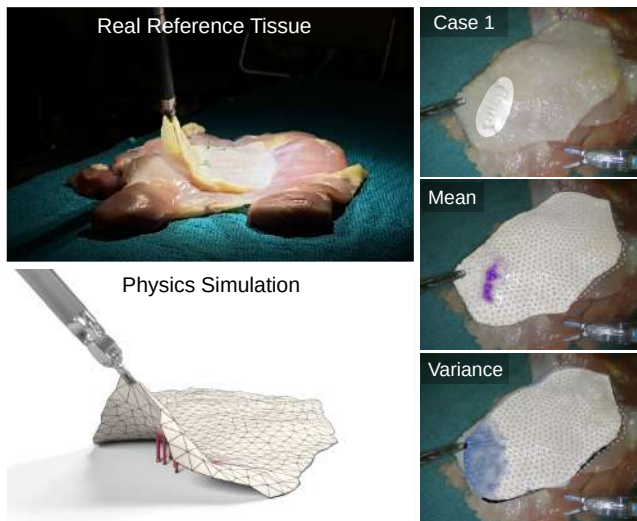


Fig. 1. JIGGLE conducts probabilistic estimation of soft tissue attachment points from image data and manipulation of the tissue. The estimated boundary, i.e. the suture locations, are shown in purple. A corresponding confidence metric is shown in blue.

the tissue. Previous approaches like [15] that consider the joint problem of estimation and active sensing are limited in the resolution of the attachment regions they can detect. Safety is not considered, and behaviors are limited to hand-tuned motion primitives. Additionally, previous works do not show their results on real tissue data and fail to consider topological changes like cutting and suturing.

In this work, our goal is to realize an interactive approach to estimating, manipulation, and tracking of a deformable thin-shell tissue for safer, more intelligent tissue control. Specifically, we propose the Joint Interactive Guided Gaussian Likelihood Estimation (JIGGLE) method: a novel active sensing framework for estimating boundary attachment points in deformable surgical environments. We leverage a differentiable physics simulator to develop an efficient probabilistic estimation framework for deformable environments with a high degree of freedom (DOF). Our estimation framework relies solely on stereo camera observations which is typically the only available feedback modality during surgery. We demonstrate the robustness of this estimation in real tissue manipulation experiments, as shown in Fig. 1. We take advantage of the probabilistic nature of the estimation framework to build an active sensing pipeline that selects actions to maximize information gain while minimizing a safety cost to avoid tissue tearing. We showcase the complete

\* denotes equal contribution. The authors are associated with University of California San Diego, La Jolla, CA 92093, USA {nshinde, x5liang, f4liu, yuz049, frichter, sherbert, yip}@ucsd.edu

JIGGLE framework in simulations involving topological changes like cutting and suturing.

## II. METHODS

**Problem Statement:** In this paper we consider a deformable thin shell tissue  $\mathcal{T}$  represented by a mesh with  $n$  particles with positions  $\mathbf{x}_t = [\mathbf{x}_t^1 \dots \mathbf{x}_t^n] \in \mathbb{R}^{n \times 3}$  at time  $t$ . A subset of the tissue  $\mathcal{T}_b \subseteq \mathcal{T}$  is attached to the environment by boundary constraints of varying strength parameterized by  $\mathbf{b}_t = [\mathbf{b}_t^1 \dots \mathbf{b}_t^n] \in \mathbb{R}^{n \times 1}$ . The tissue is controlled by moving a fixed point on the tissue with actions  $u_t \in \mathbb{R}^3$ . Our goal for the estimation task is to estimate the true boundary constraints  $\mathbf{b}^*$  given observations of a real reference tissue  $\mathcal{T}_{\text{ref}}$ . For active sensing, we aim to maximize information gain and find the best actions to estimate  $\mathbf{b}^*$ .

**Estimation:** To solve the above problem statement we represent **Extended Position-based Dynamics (XPBD)** [16]. We control the tissue with actions  $u_t$  that specify the position of an infinite-mass virtual control particle that is connected to a local neighborhood of points on the tissue mesh. We formulate our boundary constraints as zero resting length spring attachments between each tissue particle and infinite-mass virtual particles that are fixed to the tissue particle's initial resting positions  $\mathbf{x}_0 = [\mathbf{x}_0^1 \dots \mathbf{x}_0^n]$ .

We propose a probabilistic estimation framework to track boundary constraint distributions,  $\mathbf{b}_t$ , over the true boundary parameters. The differentiability of the XPBD simulation allows us to locally linearize the tissue model. This in conjunction with a multivariate Gaussian representation of  $\mathbf{b}_t \sim \mathcal{N}(\hat{\mathbf{b}}_t, \Sigma_t)$  allows us to easily track  $\mathbf{b}_t$  with an extended Kalman Filter (EKF) formulation. The motion model of our EKF describes the change in the boundary estimate  $\mathbf{b}_t$  between the time steps. We use  $\delta \mathbf{b}_t \in \mathbb{R}^n$  to represent topology-changing actions, such as suturing or cutting, that directly modify the boundary parameters.

$$\begin{aligned} \mathbf{b}_{t+1} &= m(\mathbf{b}_t, \delta \mathbf{b}_t, w_t) = \mathbf{b}_t + \delta \mathbf{b}_t + w_t \\ w_t &\sim \mathcal{N}(0, W_t) \end{aligned} \quad (1)$$

During topology changing actions  $\delta \mathbf{b}_t$  is non-zero with  $W_t$  having larger covariance values near the modified regions.

As the boundary parameters are not directly visible, we observe them indirectly through the tissue  $x_t^{\text{ref}}$ :

$$\begin{aligned} \mathbf{x}_{t+1} &= h(\mathbf{b}_{t+1}, \mathbf{x}_t^{\text{ref}}, u_t, v_t) = f(\mathbf{x}_t^{\text{ref}}, u_t, \mathbf{b}_{t+1}) + v_{t+1} \\ v_{t+1} &\sim \mathcal{N}(0, V_{t+1}) \end{aligned} \quad (2)$$

Here, we initialize the XPBD simulation,  $f$ , with the last observed tissue state,  $x_t^{\text{ref}}$ , and forward simulate with the belief the boundary constraints from the motion model.

Using equations 1 and 2 we can track the changes to the boundary parameter belief, represented by  $\hat{\mathbf{b}}_t$  and  $\Sigma_t$ .

**Prediction :**

$$\hat{\mathbf{b}}_{t+1|t} = \hat{\mathbf{b}}_{t|t} + \delta \mathbf{b}_t, \Sigma_{t+1|t} = \Sigma_{t|t} + W_t \quad (3)$$

**Update :**

$$\begin{aligned} \hat{\mathbf{b}}_{t+1|t+1} &= \hat{\mathbf{b}}_{t+1|t} + K_{t+1} \tilde{\mathbf{y}}_{t+1} \\ \Sigma_{t+1|t+1} &= (I - K_{t+1} J_{t+1}) \Sigma_{t+1|t} \end{aligned} \quad (4)$$

TABLE I

COMPARISON OF BOUNDARY ESTIMATION ACCURACY AFTER 4 GRASP SEQUENCES. RESULTS DEMONSTRATE OUR METHOD OUTPERFORMS THE BASELINE ADAM OPTIMIZER.

Cases	PCD $\uparrow$		PUG $\uparrow$	
	Adam	Ours	Adam	Ours
Arc	82.1	100	59.3	87.1
Line	85.7	100	40.0	43.3
Line-dot	68.0	96.0	34.7	48.9
Arc-line	83.8	97.3	51.8	65.5
U-shape	87.3	97.5	52.9	76.0

where the observation residual  $\tilde{\mathbf{y}}_{t+1}$ , and the Kalman gain  $K_{t+1}$  are given by:

$$\begin{aligned} \tilde{\mathbf{y}}_{t+1} &= \mathbf{x}_{t+1}^{\text{ref}} - h(\hat{\mathbf{b}}_{t+1|t}, \mathbf{x}_t^{\text{ref}}, u_t, v_t) \\ K_{t+1} &= \Sigma_{t+1|t} J_{t+1}^\top S_{t+1}^{-1} \end{aligned} \quad (5)$$

with the residual covariance  $S_{t+1}$ , the observation Jacobians  $J_{t+1}$ , and covariance Jacobians  $R_{t+1}$  as:

$$\begin{aligned} S_{t+1} &= J_{t+1} \Sigma_{t+1|t} J_{t+1}^\top + R_{t+1} V_{t+1} R_{t+1}^\top \\ R_{t+1} &= \left. \frac{\partial h}{\partial v} \right|_{\hat{\mathbf{b}}_{t+1|t}} = I \\ J_{t+1} &= \left. \frac{\partial h}{\partial \mathbf{b}} \right|_{\hat{\mathbf{b}}_{t+1|t}} = \left. \frac{\partial f(\mathbf{x}_t^{\text{ref}}, u_t, \mathbf{b}_{t+1})}{\partial \mathbf{b}} \right|_{\hat{\mathbf{b}}_{t+1|t}} \end{aligned} \quad (6)$$

Here,  $f(\mathbf{x}_t^{\text{ref}}, \hat{\mathbf{b}}_{t+1|t}, u_t)$  outputs the expected tissue surface after using the XPBD simulator to forward simulate one timestep with action  $u_t$ , using the mean of the current estimated boundary belief,  $\hat{\mathbf{b}}_{t+1|t}$ . To enhance the robustness of our estimation, we modify the EKF to use  $k$  uniform samples of previous observations up until the last topology changing action. We use the multiple shooting method to encode previous observations [17]; this approach samples from previously observed trajectories, forward simulates from those samples using the current belief and penalizes the deviation of predicted particle states from the reference observations. To get accurate observations of the tissue state,  $x_t^{\text{ref}}$ , for real world experiments, we introduce an observation-matching condition into the XPBD simulation's iterative constraint solving procedure, similar to [18]. As this condition uses the current boundary constraint estimate,  $\mathbf{b}_t$ , we combine the EKF update and state estimation into one joint estimation problem where both are iteratively estimated.

**Active Sensing:** For the active sensing problem, we want to solve for actions that minimize the entropy of the boundary constraint belief distribution,  $\mathbf{b}_t$ , while minimizing the boundary energy to prevent the tissue from experiencing unsafe forces. In place of the computationally complex entropy minimization objective we introduce a heuristic to maximize  $\mathcal{D}$ : Uncertainty-Weighted Displacement (UWD).

$$\mathcal{D}(\mathbf{x}_t^{\text{ref}}, u_t, \hat{\mathbf{b}}_t) = \left\| \widehat{\Delta \mathbf{x}_{t+1}} \cdot \Sigma_t \right\| \quad (7)$$

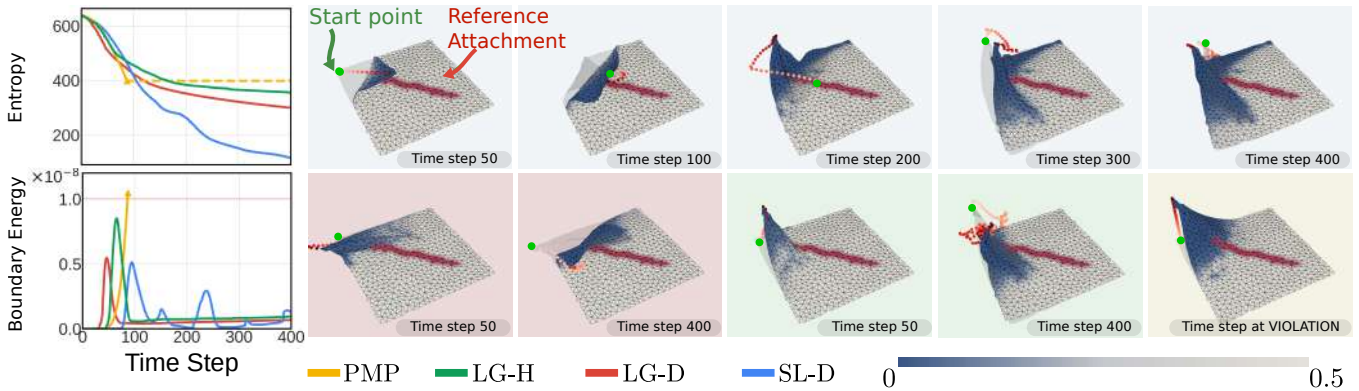


Fig. 2. Results from our active sensing experiments with 4 different strategies: SL-D (blue) is our method, LG-H (green) and LG-D (red) are local gradient variations of our method, and PMP (yellow) is a baseline. The red color on the tissue highlights the reference attachment, and the blue shows the confidence, inverse of variance, of the estimated boundary. The dotted line in the boundary energy graph denotes the safety threshold. SL-D achieves more entropy reduction than all other baselines while keeping a safe boundary energy profile. In comparison, local controllers LG-H and LG-D get trapped in local minima, resulting in higher entropy. PMP results in quick safety violations. Additional active sensing results can be found in Fig. 7 of the appendix.

$$\begin{aligned} \mathbf{x}_{t+1} &= f(\mathbf{x}_t^{\text{ref}}, u_t, \hat{\mathbf{b}}_{t+1|t}), \Delta \mathbf{x}_{t+1} = \mathbf{x}_{t+1} - \mathbf{x}_0 \\ \widehat{\Delta \mathbf{x}}_{t+1} &= \sum_i^n \mathbf{e}_i \mathbf{e}_i^\top \otimes [\Delta \mathbf{x}_{t+1}]_i. \end{aligned} \quad (8)$$

Here  $\mathbf{e}_i$  is the  $i^{\text{th}}$  standard basis vector and  $\otimes$  is the kronecker product. This effectively maximizes information gain by encouraging more displacement in regions that are more uncertain as weighted by  $\Sigma_t$ . We prevent unsafe actions by adding objectives to minimize the energy on the tissue's boundary constraints and limit the range of the actions.

Optimizing the above objectives for the best actions using a local gradient based controller suffers from local minima as well as vanishing gradient issues. Evaluating a multi-step trajectory also imposes computational challenges. To address these challenges we introduce a sampling-based large step controller. We first uniformly sample several large-step control actions. We refine these actions through gradient step updates with respect to the optimization objectives. We then select the action that best optimizes our objective before taking a small step in its direction and re-planning. We encourage smoothness by carrying over the top 10 samples across each sampling iteration.

### III. RESULTS AND EVALUATION

We evaluate our estimation method in simulation over 5 different environments. We repeat 4 grasp sequences on the 4 corners of the tissue while running our estimation framework. We record the percentage of correct detections of attachment points (PCD) and the percentage of the uncovered ground truth (PUG). Table I summarizes our results with our method performing the baseline of updating the boundary parameters using gradient updates: "adam". The environments and experiments are visualized in Fig. 5 and 6 in the appendix.

We also evaluate our estimation framework in a real world experiment shown in Fig. 1 and Fig. 8 in the appendix. We create boundary constraints by suturing chicken skin to a chicken thigh. We are able to successfully recover the tissue's boundary constraints from endoscopic camera observations of manipulating the tissue using tweezers. We compare the

TABLE II  
REAL WORLD ESTIMATION RESULTS. THE NUMBER AFTER THE METRICS CORRESPONDS TO THE DILATION FACTOR APPLIED.

	PCD $\uparrow$	PCD-1	PCD-2	PUG $\uparrow$	PUG-1	PUG-2
Case1-BANet	0	0	0	0	0	0
Case1-Adam	46.2	<b>84.6</b>	84.6	54.5	100.0	100.0
Case1-Ours	<b>47.4</b>	84.2	<b>89.5</b>	<b>81.8</b>	100.0	100.0
Case1-Ours- $\sigma=0.1$	60	93.3	100	81.8	100.0	100.0
Case2-BANet	0	0	7.1	0	0	7.5
Case2-Adam	0.0	2.1	10.4	0.0	2.5	17.5
Case2-Ours	<b>33.3</b>	<b>83.3</b>	<b>100.0</b>	<b>5.0</b>	<b>27.5</b>	<b>37.5</b>
Case2-Ours- $\sigma=0.1$	40.0	100	100.0	11.1	55.6	72.2

PCD and PUG of our method, "adam" baseline and BANet [19] in Table II. Visual comparisons can be found in Fig. 9

To evaluate active sensing, we compare four different variants of our proposed framework:

- 1) **LG-H**: Local gradient-based action, minimizing entropy. Only refines actions with local gradient based updates.
- 2) **LG-D**: Local gradient-based, maximizing displacement
- 3) **SL-D**: Our proposed method
- 4) **PMP**: Predefined motion primitives: An exhaustive search to minimize entropy over motion primitives of  $(\pm x, \pm y, \pm z)$ . [15]

Our method, SL-D, consistently achieves greater entropy reduction while keeping a safe boundary energy profile. Results of this are shown in Fig. 2. Using motion model  $m$ , our framework can also handle topological changes, and be used to estimate the success of suturing or cutting. Examples of these procedures are shown Fig. 4 and 3 in the appendix.

### IV. CONCLUSION

In this paper we proposed a novel framework for active sensing and boundary parameter estimation in deformable surgical environments. We demonstrated the estimation capabilities of our method in both simulation and real world experiments. Our active sensing experiments showcased our method's ability to manipulate the tissue to maximize information gain while respecting safety constraints.

## REFERENCES

- [1] P. Kazanzides, Z. Chen, A. Deguet, G. S. Fischer, R. H. Taylor, and S. P. DiMaio, "An open-source research kit for the da vinci® surgical system," in *2014 IEEE International Conference on Robotics and Automation (ICRA)*, 2014, pp. 6434–6439.
- [2] A. Shademan, R. S. Decker, J. D. Opfermann, S. Leonard, A. Krieger, and P. C. W. Kim, "Supervised autonomous robotic soft tissue surgery," *Science Translational Medicine*, vol. 8, no. 337, pp. 337ra64–337ra64, 2016. [Online]. Available: <https://www.science.org/doi/abs/10.1126/scitranslmed.aad9398>
- [3] Z. Hu, T. Han, P. Sun, J. Pan, and D. Manocha, "3-d deformable object manipulation using deep neural networks," *IEEE Robotics and Automation Letters*, vol. 4, no. 4, pp. 4255–4261, 2019.
- [4] B. P. Murphy and F. Alambeigi, "A surgical robotic framework for safe and autonomous data-driven learning and manipulation of an unknown deformable tissue with an integrated critical space," *Journal of Medical Robotics Research*, vol. 8, no. 01n02, p. 2340001, 2023.
- [5] B. Thach, B. Y. Cho, A. Kuntz, and T. Hermans, "Learning visual shape control of novel 3d deformable objects from partial-view point clouds," in *2022 International Conference on Robotics and Automation (ICRA)*. IEEE, 2022, pp. 8274–8281.
- [6] Z. Chiu, A. Z. Liao, F. Richter, B. Johnson, and M. C. Yip, "Markerless suture needle 6d pose tracking with robust uncertainty estimation for autonomous minimally invasive robotic surgery," *CoRR*, vol. abs/2109.12722, 2021. [Online]. Available: <https://arxiv.org/abs/2109.12722>
- [7] H. Saeidi, H. N. D. Le, J. D. Opfermann, S. Leonard, A. Kim, M. H. Hsieh, J. U. Kang, and A. Krieger, "Autonomous laparoscopic robotic suturing with a novel actuated suturing tool and 3d endoscope," in *2019 International Conference on Robotics and Automation (ICRA)*, 2019, pp. 1541–1547.
- [8] F. Richter, S. Shen, F. Liu, J. Huang, E. K. Funk, R. K. Orosco, and M. C. Yip, "Autonomous robotic suction to clear the surgical field for hemostasis using image-based blood flow detection," *IEEE Robotics and Automation Letters*, vol. 6, no. 2, pp. 1383–1390, 2021.
- [9] B. Thananjeyan, A. Garg, S. Krishnan, C. Chen, L. Miller, and K. Goldberg, "Multilateral surgical pattern cutting in 2d orthotropic gauze with deep reinforcement learning policies for tensioning," in *2017 IEEE International Conference on Robotics and Automation (ICRA)*, 2017, pp. 2371–2378.
- [10] J. Ge, M. Kam, J. D. Opfermann, H. Saeidi, S. Leonard, L. J. Mady, M. J. Schnermann, and A. Krieger, "Autonomous system for tumor resection (astr) - dual-arm robotic midline partial glossectomy," *IEEE Robotics and Automation Letters*, vol. 9, no. 2, pp. 1166–1173, 2024.
- [11] Y. Li, F. Richter, J. Lu, E. K. Funk, R. K. Orosco, J. Zhu, and M. C. Yip, "Super: A surgical perception framework for endoscopic tissue manipulation with surgical robotics," *IEEE Robotics and Automation Letters*, vol. 5, no. 2, p. 2294–2301, Apr. 2020. [Online]. Available: <http://dx.doi.org/10.1109/LRA.2020.2970659>
- [12] S. Lin, A. J. Miao, J. Lu, S. Yu, Z.-Y. Chiu, F. Richter, and M. C. Yip, "Semantic-super: A semantic-aware surgical perception framework for endoscopic tissue identification, reconstruction, and tracking," in *2023 IEEE International Conference on Robotics and Automation (ICRA)*, 2023, pp. 4739–4746.
- [13] Y. Long, Z. Li, C. H. Yee, C. Ng, R. H. Taylor, M. Unberath, and Q. Dou, "E-DSSR: efficient dynamic surgical scene reconstruction with transformer-based stereoscopic depth perception," *CoRR*, vol. abs/2107.00229, 2021. [Online]. Available: <https://arxiv.org/abs/2107.00229>
- [14] Y. Wang, Y. Long, S. H. Fan, and Q. Dou, "Neural rendering for stereo 3d reconstruction of deformable tissues in robotic surgery," in *International conference on medical image computing and computer-assisted intervention*. Springer, 2022, pp. 431–441.
- [15] P. Boonvisut and M. C. Çavuşoğlu, "Identification and active exploration of deformable object boundary constraints through robotic manipulation," *The International journal of robotics research*, vol. 33, no. 11, pp. 1446–1461, 2014.
- [16] M. Macklin, M. Müller, and N. Chentanez, "Xpbd: position-based simulation of compliant constrained dynamics," in *Proceedings of the 9th International Conference on Motion in Games*, 2016, pp. 49–54.
- [17] E. Heiden, C. E. Denniston, D. Millard, F. Ramos, and G. S. Sukhatme, "Probabilistic inference of simulation parameters via parallel differentiable simulation," in *2022 International Conference on Robotics and Automation (ICRA)*. IEEE, 2022, pp. 3638–3645.
- [18] X. Liang, F. Liu, Y. Zhang, Y. Li, S. Lin, and M. Yip, "Real-to-sim deformable object manipulation: Optimizing physics models with residual mappings for robotic surgery," *arXiv preprint arXiv:2309.11656*, 2023.
- [19] E. Tagliabue, D. Dall'Alba, M. Pfeiffer, M. Piccinelli, R. Marin, U. Castellani, S. Speidel, and P. Fiorini, "Data-driven intra-operative estimation of anatomical attachments for autonomous tissue dissection," *IEEE Robotics and Automation Letters*, vol. 6, no. 2, pp. 1856–1863, 2021.

## V. APPENDIX

We show additional results of our method in the appendix. Fig. 4 and Fig. 3 illustrate examples of our framework used during topological changes like suturing and cutting respectively. Fig. 5 and Fig. 6 show the simulation environments used to evaluate our estimation framework as well as examples of our estimation experiments respectively. Additional active sensing experiments across different environments are shown in Fig. 7. All the estimation results from our real world test cases are visualized in Fig. 8. Fig. 9 shows visual comparison results between our method the baseline and existing approaches. The corresponding quantitative results for all these real world experiments are summarized in Table III.

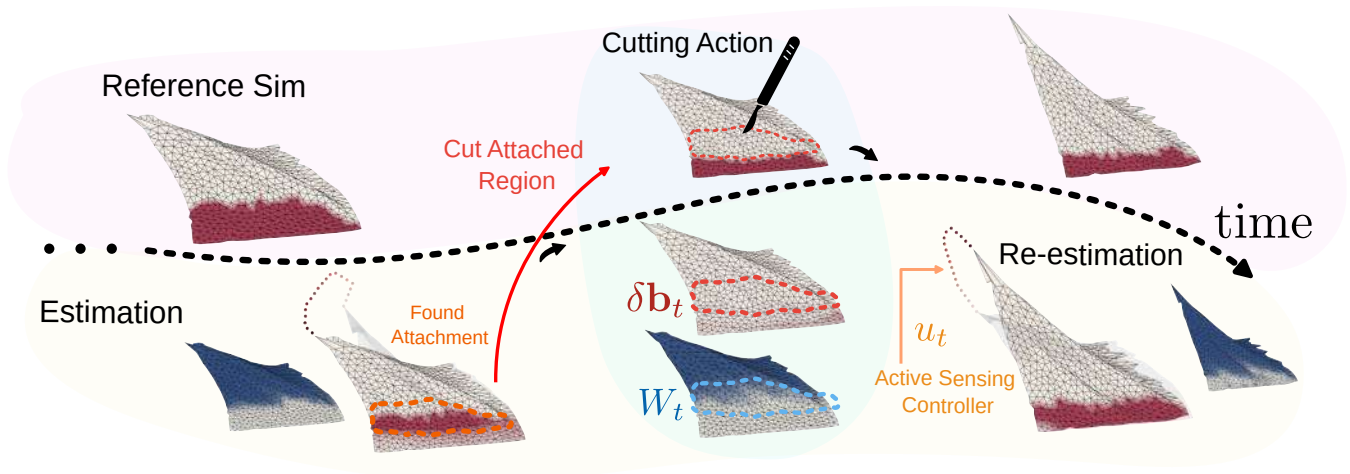


Fig. 3. We applied JIGGLE to a tissue detachment procedure on test case *Large-attach*, which is done by iteratively applying the active sensing approach to find the attachment points, and then a cut is made at that discovered boundary. The sequence of images depicts an iteration of this procedure where the top row shows the ground-truth boundary attachment in red, and the bottom row shows our estimation of the boundary in red and the confidence, inverse of variance, in blue. After each cut action is applied, where all of the discovered boundary is removed, the cutting information,  $\delta \mathbf{b}_t, W_t$ , is also fed into our estimation algorithm. The strategy is repeated until the tissue is fully detached and it took 7 cycles in this experiment to detach the tissue successfully

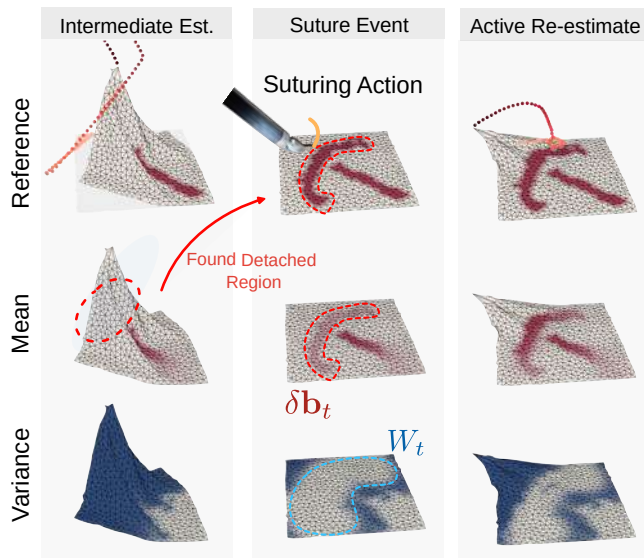


Fig. 4. We applied JIGGLE to a suturing procedure by 1) the left column: applying the active sensing approach to find where the tissue is detached, 2) the middle column: applying a suture action at the desired detached area, and 3) the right column: active sensing again to validate the suture action. The top row of images shows the ground truth attachment in red, and the bottom row shows our estimation of the boundary in red and the confidence, inverse of variance, in blue. After each suture is applied, the suture information is also fed into our estimation algorithm, including a noise injection near the suture region, so the active sensing policy is encouraged to confirm where the new boundary has been added. The second re-estimation, confirming the boundary after the suture, reports an increase in PUG from 20.2 to 75.2. The PCD value remains the same at 100, indicating no false detections.

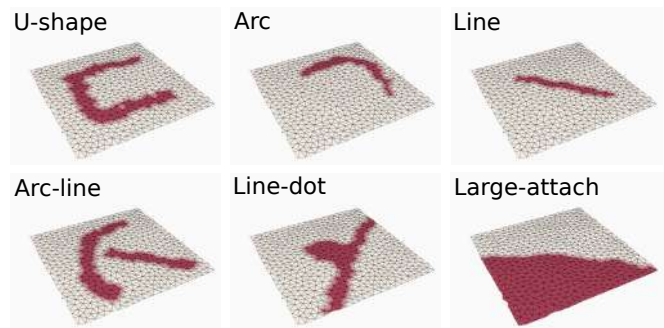


Fig. 5. The images show the ground truth attachment points in red using spring boundary constraints for the simulation test cases in our experiments.

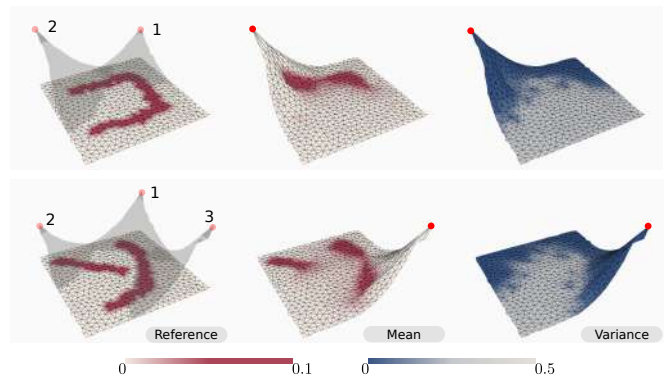


Fig. 6. Example results from our estimation framework on simulated environments where the order of the grasps is numbered, and the boundary is highlighted in red on the left-most column. The final result from our proposed method is shown in red in the middle column. Finally, the confidence (inverse of variance) of our estimation is shown in blue in the rightmost column. We can see how the variance has decreased in the regions where the trajectories have displaced the tissue from its original state, and the mean estimate has converged close to the reference values.

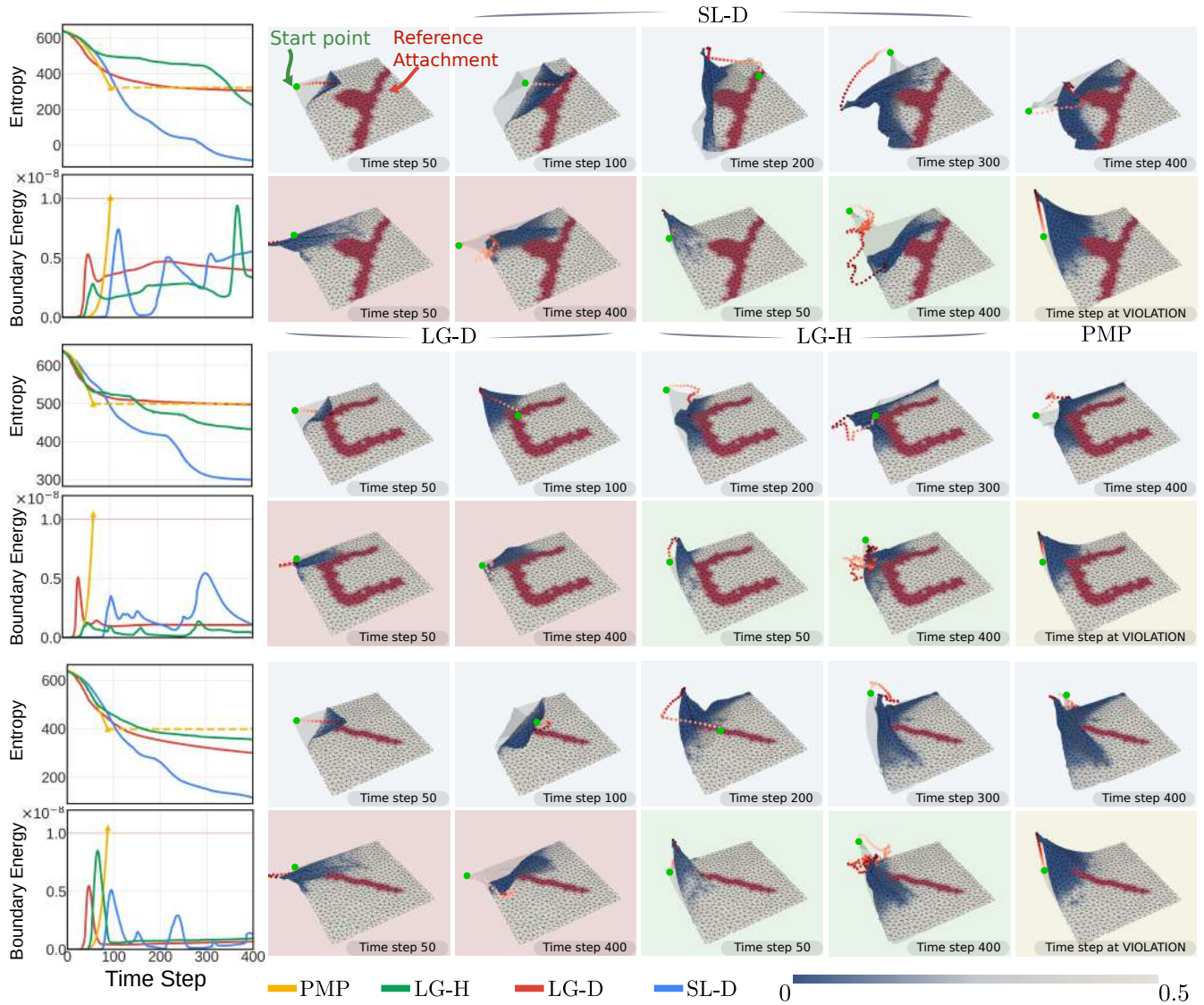


Fig. 7. Results from our active sensing experiments with 4 different strategies: PMP (yellow) is a baseline, and SL-D (blue), LG-H (green), and LG-D (red) are proposed in this work. Every two rows show one experiment with the entropy and energy plotted in the left-most column, and the images on the right show a collage of the control trajectories being applied from the different active sensing strategies. Note that the colored background on each image corresponds to the active sensing strategy (best viewed in color). The red color on the tissue highlights the reference attachment, and the blue shows the confidence, inverse of variance, of the estimated boundary. The goal of the active sensing strategies is to maximize the confidence, which is measured in entropy, while adhering to safety constraints, which are measured in energy. Overall, SL-D achieves more entropy reduction than all other baselines while keeping a safe boundary energy profile. It also produces the most intricate control point trajectories, such as switching directions and folding. In comparison, local controllers LG-H and LG-D get trapped in local minima, resulting in higher entropy. PMP reduces entropy in the beginning but results in quick safety violations.

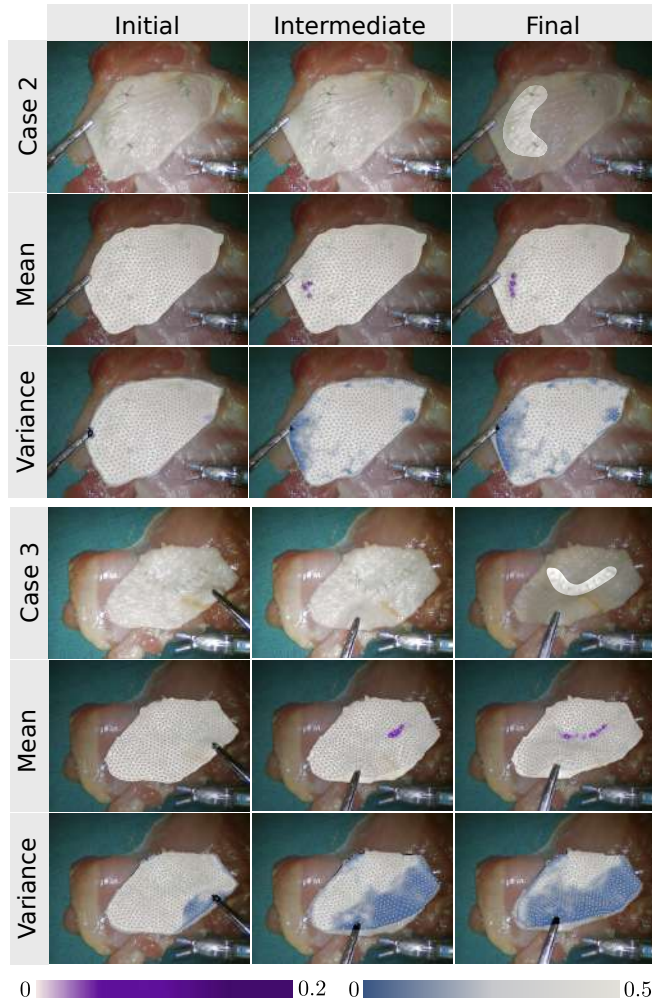


Fig. 8. This figure shows results from real-world tissue attachment point estimation experiments case 2 and case 3 (case 1 is shown in Fig. 1). Time progresses from left to right. A dark purple value corresponds to a stronger estimated attachment point, and a darker blue value corresponds to lower uncertainty about the boundary parameters at that region. Notice that as the tissue is deformed, the variance decreases, and the estimated mean of our boundary matches closer to the ground truth.

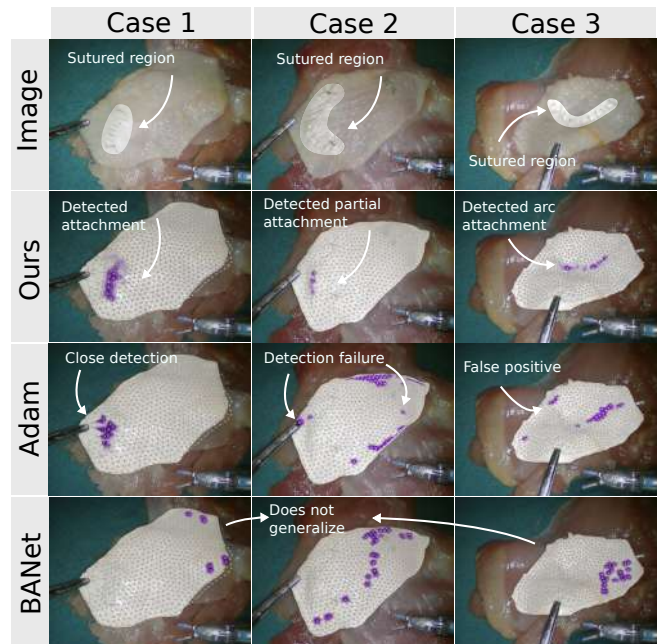


Fig. 9. Detailed comparison of estimated attachment points between the proposed method and the Adam optimizer. In the second row, our method successfully detects attachment shape. In comparison, the Adam optimizer estimates predictions that are close to the true region (case 1) but fails in other cases, producing many false positive estimations. Because BANet cannot generalize to our real-world data, it fails to predict meaningful results.

TABLE III

RESULTS FROM OUR REAL WORLD ESTIMATION EXPERIMENT. THE NUMBER AFTER THE METRICS CORRESPONDS TO HOW MUCH DILATION IS APPLIED WHEN COMPUTING THE METRIC.

	PCD $\uparrow$	PCD-1	PCD-2	PUG $\uparrow$	PUG-1	PUG-2
Case1-BANet	0	0	0	0	0	0
Case1-Adam	46.2	<b>84.6</b>	84.6	54.5	100.0	100.0
Case1-Ours	<b>47.4</b>	84.2	<b>89.5</b>	<b>81.8</b>	100.0	100.0
Case1-Ours- $\sigma=0.1$	60	93.3	100	81.8	100.0	100.0
Case2-BANet	0	0	7.1	0	0	7.5
Case2-Adam	0.0	2.1	10.4	0.0	2.5	17.5
Case2-Ours	<b>33.3</b>	<b>83.3</b>	<b>100.0</b>	<b>5.0</b>	<b>27.5</b>	<b>37.5</b>
Case2-Ours- $\sigma=0.1$	40.0	100	100.0	11.1	55.6	72.2
Case3-BANet	8.0	20.0	32.0	4.2	14.5	22.5
Case3-Adam	<b>45.2</b>	61.3	67.7	<b>42.4</b>	<b>81.8</b>	97.0
Case3-Ours	44.5	<b>72.2</b>	<b>88.9</b>	24.2	78.8	<b>100.0</b>
Case3-Ours- $\sigma=0.1$	40.0	70.0	100.0	14.8	37.0	63.0